Advances in Structural Engineering

Advances in Structural Engineering
2025, Vol. 0(0) 1–23

DOI: 10.1177/13694332251340715
journals.sagepub.com/home/ase
Sage

Temperature-based structural identification of long-span bridges using InSAR observation and meteorological shared data

Yun Zhou[1], Xiaowan Xu[1], Guanwang Hao[1], Ziqing Wei[1], Yingao Liu[1] and Fan Yi[2]

Abstract

The Interferometric Synthetic Aperture Radar (InSAR) technology can be used for the health monitoring of long-span bridges, capable of measuring bridge deformations with millimeter-level precision. It is particularly effective for monitoring long-period temperature-induced deformations, providing valuable insights into abnormal changes in structural properties. However, few studies have focused on evaluating the condition of in-service bridges based on obtained deformations. Therefore, this paper adopts a temperature-based structural identification (TBSI) theory combined with InSAR technology for damage diagnosis in bridge regions. On this basis, the bridge structural temperature calculated from meteorological shared data and the displacement obtained through InSAR technology are used as the input and output, respectively, followed by an updated finite element model (FEM) of the bridge established for thermal-structural coupling analysis. The Differential Evolution (DE) algorithm is then applied to identify regions with abnormal thermal expansion coefficients, facilitating the localization and quantification of bridge damage. A case study of a long-span suspension bridge exemplifies the application of the proposed method, validating its accuracy in identifying assumed damaged regions and reflecting the structural health status, with damage quantification errors within 5%. This method provides an effective approach for the lightweight monitoring of bridge health.

Keywords

bridge health monitoring, temperature-based structural identification, InSAR, finite element model updating, damage identification, thermal-structural coupling analysis

Introduction

Long-span bridges are critical components of transportation infrastructure for guaranteeing regional economic development. According to the *2023 Statistical Bulletin on the Development of the Transportation Industry* released by the Ministry of Transport (MOT), China had 1.0793 million highway bridges by the end of 2023, including 10,239 super-large bridges and 177,700 large bridges (MOTOC, 2024). However, environmental factors such as solar radiation, air temperature, wind speed, and other conditions could cause significant variations in temperature distribution across bridges (Zuk, 1965). This non-uniform temperature distribution remarkably affects the mechanical performance of bridge structures, resulting in the deterioration of load-bearing capacity and even structural failures (Dilger et al., 1983; Han et al., 2021b; Zhou et al., 2020).

Existing research indicates that long-period bridge deformations, predominantly attributed to temperature effects, exhibit displacements which may exceed those caused by structural damage or operational loads (Li et al., 2023; Xu et al., 2010; Zhou et al., 2021). The heat exchange between bridges and external environments is the main cause of temperature effects on bridges. Zhou et al. (2024) reviewed the factors and methods for calculating bridge temperature, summarizing convective heat transfer, radiation mechanisms, and related theoretical and experimental approaches. To account for temperature effects, some researchers have investigated the correlation between temperature data measured at

[1]College of Civil Engineering, Hunan University, Changsha, China
[2]College of Civil Engineering, Changsha University, Changsha, China

Corresponding author:
Guanwang Hao, College of Civil Engineering, Hunan University, Changsha 410082, China.
Email: gwh0114@hnu.edu.cn

limited sensor points in structural health monitoring (SHM) systems and structural responses to identify structural damage and assess stiffness degradation (Kromanis and Kripakaran, 2016; Wang et al., 2022; Xia et al., 2020; Yang et al., 2018; Zhu et al., 2021). Data from instrumented sensors on bridges have shown that the correlation between temperature and girder deflections can be used to identify changes in structural stiffness parameters. Building on this, Zhou et al. (2020) proposed an analytical solution to temperature-induced deformation in suspension bridges, further exploring how temperature variations can influence bridge deflections. Based on numerical simulations of long-span suspension bridges, Xia et al. (2017) identified the stiffness of main girders and further assessed structural damage by analyzing temperature and temperature-induced strains. Similarly, Sun et al. (2019) proposed a real-time damage identification method for bridge SHM that accounts for temperature variations, utilizing finite element model (FEM), partial least-squares regression, and a fusion of global inclination and local strain data.

Interferometric Synthetic Aperture Radar (InSAR), as one of the technologies capable of monitoring bridge structural deformations, serves as a key tool for assessing and providing early warning of the health status of bridge structures. InSAR is a radar technology capable of detecting millimeter-level deformations in long-span bridges (Zhou et al., 2024), enabling long-term deformation monitoring of these bridges without installing any sensors. Therefore, InSAR is a lightweight and efficient approach for SHM, offering a non-invasive solution that minimizes the need for on-site sensor installation. The InSAR technology can identify the quasi-static temperature deformation information from relatively stable targets, i.e., Persistent Scatterers (PS), on the bridge structure. Huang et al. (2017) employed Persistent Scatterer Interferometry (PSI) technology to monitor the displacement of a high-speed railway bridge and compared the PSI-measured displacements with field measurements. Qin et al. (2018b) proposed a method that integrates the Point-like Targets selection strategies of PS and small baseline interferometric processing, effectively improving the robustness of deformation estimation for cable-stayed bridges. Caspani et al. (2023) extracted displacements of a highway bridge and studied their correlation with environmental phenomena employing PSI method, particularly changes in temperature and river flow. Additionally, the structural movement velocity obtained from displacement time series derived from PSI can serve as an indicator for bridge safety assessment. By combining displacement data obtained through InSAR with structural and collapse analysis from Farneti et al. (2023), potential critical conditions can be identified, and the failure time of bridges experiencing slow landslide-induced movements can be predicted. The feasibility of PSI method for long-term deformation monitoring of bridges has been effectively verified in previous studies. This non-contact measurement method eliminates the need for installing extensive equipment on structures, simplifying the monitoring process and enabling lightweight long-term monitoring. However, its application in structural damage assessment remains limited.

The paradigm of structural identification (St-Id) aims to bridge the gap between mathematical models and real-world systems by correlating simulation models with experimental data to estimate structural performance and vulnerability (Catbas et al., 2010), offering a potential means for bridge damage assessment through InSAR-measured displacements. St-Id methods are categorized based on different excitation approaches and response characteristics, including static-based, dynamic-based, and temperature-based methods (Yi, 2021). Numerous studies have been conducted using static data for structural damage identification. Sanayei and Scampoli (1991) proposed a finite element (FE)-based method that provides valuable insights for static parameter identification. In this method, static test data is utilized for detecting stiffness degradation in bridge decks, and the Monte Carlo method is applied to correct measurement errors. Cai et al. (2004) developed a probabilistic analysis method for structural damage detection and condition assessment based on static St-Id. Static-based St-Id is employed to reveal various types of information, including the composite action of the deck and main girders (Breña et al., 2013), live load distribution factors (Barr et al., 2001), span continuity (James, 2016; James and Yarnold, 2017), load ratings (Bell et al., 2013), and load carrying capacity (Chajes, 2006). In recent years, some researchers have integrated the static-based St-Id method with artificial intelligence algorithms, leading to new research explorations. Kourehli et al. (2013) utilized simulated annealing algorithms to solve objective functions derived from modal data and static displacements, aiming to locate and quantify damage in beam and frame structures. Wu et al. (2024) introduced a stiffness identification method combining the Mayfly algorithm and static displacement response surfaces. With optimization algorithms, these methods effectively quantified damage, while others lacking such support failed to assess damage extent. The static deflection-based St-Id method typically requires controlled load tests under one-off periodic monitoring, which is challenging for continuous monitoring of in-service structures.

In dynamic-based St-Id methods, frequencies, mode shapes and their derivatives (e.g., modal curvatures) are generally used as dynamic features (Yi, 2021). Most damage-related information can be extracted by analyzing vibration data (Chen et al., 2017; Cho and Cho, 2022; Sadhu et al., 2017; Yanez-Borjas et al., 2020). These studies focus solely on dynamic data for St-Id, whereas later studies utilize FEMs for dynamic St-Id. Rainieri and Fabbrocino (Rainieri et al., 2011; Rainieri and Fabbrocino, 2015) automated the extraction of modal parameters from SHM system measurement data, and subsequently utilized these dynamic parameters as inputs for structural damage identification through a modal-based damage detection algorithm. From these vibration measurements, the true structural model can be obtained through various parameter estimation techniques (Qin SQ et al., 2018a). For example, Bacinskas et al. (2013) used dynamic load testing to calibrate the model of a single-span steel-concrete composite railway bridge. However, relevant tests are challenging in practice since exciting a bridge requires extensive instrumentations and traffic disruptions (Siringoringo and Fujino, 2008). Additionally, damage identification based on dynamic characteristics is highly susceptible to external environmental interferences (e.g., temperature, noise, and nearby vibrations), which may degrade measurement data quality and compromise the accuracy of St-Id.

The temperature-based structural identification (TBSI) method, proposed by Yarnold (Yarnold et al., 2015), is a quantitative evaluation framework that relies on temperature-induced structural responses (e.g., strain and displacement) by combining monitoring data with actual FEMs. One key advantage of TBSI lies in its ability to enable continuous, long-term monitoring with minimal intervention, as temperature serves as an easily measurable input. Moreover, temperature-induced responses are often substantial and relatively easy to measure (Murphy and Yarnold, 2018). Building on Yarnold's concept, (Han et al., 2021a)achieved accurate damage identification by updating damage parameters in FEMs utilizing temperature and temperature-induced strain. TBSI theory effectively addresses a major limitation of InSAR technology: the inability to assess damage in in-service bridges solely through deformation measurements.

To the best of the author's knowledge, structural damage assessment has been underexplored in previous studies using InSAR technology on long-span bridges. Therefore, this paper applies the TBSI theory to assess bridge safety and proposes a method for detecting and quantifying damage. An interfaced approach using MATLAB and ANSYS is employed to identify key parameters (thermal expansion coefficients), with air temperature and InSAR displacement data serving as the input and output, respectively. The model integrates actual measurement data to update the FEM and utilizes meteorological shared data to estimate structural temperature. The combination of temperature and deformation data through TBSI theory offers new possibilities for cost-effective structural assessment.

Methodology

St-Id theory

St-Id methods are typically categorized into three main types: static-based, dynamic-based, and temperature-based methods (Yi, 2021). Static-based methods usually evaluate structural properties such as stiffness through measured deformation responses under static loads. Dynamic-based methods focus on vibration responses under dynamic excitation to determine modal parameters, thereby identifying and assessing structural physical characteristics, such as stiffness. TBSI methods analyze the influence of temperature variations on structural behavior, considering material thermal expansion and contraction. Structural changes can be identified by analyzing temperature inputs and temperature-induced deformation outputs. For clarity in explaining the TBSI principles, a simplified analytical framework is adopted in subsequent demonstrations: (1) an indeterminate beam model is employed, as free thermal deformation in determinate systems cannot generate measurable internal forces essential for St-Id; (2) uniform temperature distribution is assumed to decouple thermal expansion effects from gradient-induced complexities. These controlled simplifications facilitate explicit formulation of the temperature-deformation relationship while preserving methodological transparency for readers.

The interrelationship between these excitation methods, response characteristics, and the structure itself is often referred to as the "Input," "Output," and "System" (the three elements). For clarity, this paper employs a beam model to elucidate the three scenarios of St-Id under the three excitation methods, with specific comparisons shown in Table 1.

For Scenario 1 and Scenario 2, theoretically, the structural physical properties can be solved using an inverse problem-solving approach with both input and output information; in some cases, the output alone is sufficient to conduct condition assessment. These methods facilitate the identification of structural physical parameters and damage diagnosis. For Scenario3, the theoretical TBSI process consists of six steps, as outlined below. The process for each step is illustrated in Figure 1.

Step 1: Observation & Conceptualization. Gather detailed information, such as geographic and meteorological data and structural drawings about the bridge.

Step 2: An a Priori FE Modeling. Develop a preliminary FEM under ideal conditions based on Step 1.

Table 1. Comparison of the three scenarios of St-Id under different excitation methods.

Scenario	Input	Output	System	Key system parameters
1	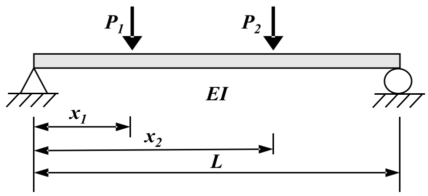 Static load	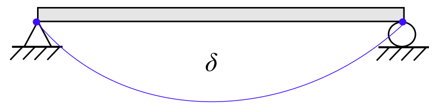 Displacements or strains	Beam/bridge/ frame	Stiffness (*EI*)
2	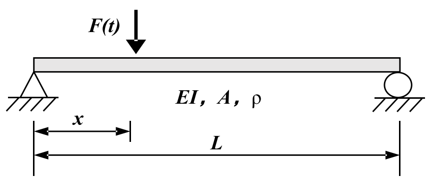 Dynamic load	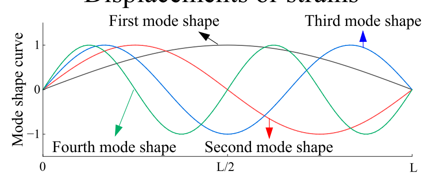 Mode shapes or frequencies	Beam/bridge/ frame	Stiffness (*EI*)
3	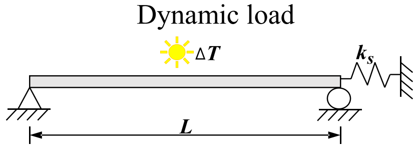 Temperature effect	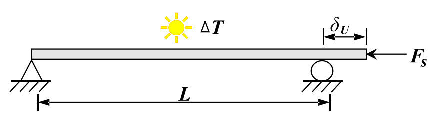 Displacements or strains	Beam/bridge/ frame	Thermal expansion coefficient (α)

Note: In Scenario 1: P_1 and P_2 represent static loads; L is the total length of the beam; x_1 and x_2 are the locations of application; *EI* is the stiffness; δ is the displacement under static loads. In Scenario 2: *F(t)* represents the dynamic load; x is the locations of application; A and ρ are the cross-sectional area and density, respectively. In Scenario 3: ΔT represents the uniform temperature; k_s is the spring stiffness; δ_U is the displacement caused by the combined effect of the equivalent spring force F_S and ΔT.

Step 3: Temperature-Based Experiment Validation. Install a SHM system and corner reflectors (CR) for validation. Identify meteorological stations near the target bridge to collect temperature data, and utilize satellite data from InSAR technology to capture temperature-induced deformation of the bridge.

Step 4: Processing & Interpretation of Data. Perform quality checks on raw data, remove external influences, and extract thermal response data.

Step 5: Temperature-Based Model Updating. Calibrate the model using temperature-driven deflection (or strain) data and FEM results, adjusting uncertain parameters based on sensitivity analysis.

Step 6: Utilization of Model for Simulations. Use the optimized model to analyze the bridge's behavior and identify potential damage.

The basic principles of TBSI taking a simply supported beam as an example are illustrated as follows. Under the uniform temperature variation ΔT, for a simply supported beam with an elastic modulus E, cross-sectional area A, thermal expansion coefficient α, and original length L, the thermal expansion of the beam results in a free elongation δ_T and free thermal strain ε_T. The deformations can be illustrated with a diagram, as shown in Figure 2(b). These deformations can be represented as (Yarnold et al., 2015):

$$\delta_T = \varepsilon_T L = \alpha(\Delta T)L \tag{1}$$

Under uniform temperature changes, a simply supported beam with unconstrained components will only experience free thermal strain without generating any associated stress. Thermal stress is generated by boundary constraints that restrict thermal deformation. To better illustrate the principle of TBSI, a simply supported beam model with a longitudinal spring support at one end is considered, as shown in Figure 2(c). It is assumed that the spring is a linear spring system with spring stiffness k_s.

This model is indeterminate. When studying its deformation under uniform temperature changes, the spring is removed and treated as a redundant reaction force applied at the right end of the simply supported beam. The constrained strain ε_R and deformation δ_R caused by the equivalent spring force can both be obtained

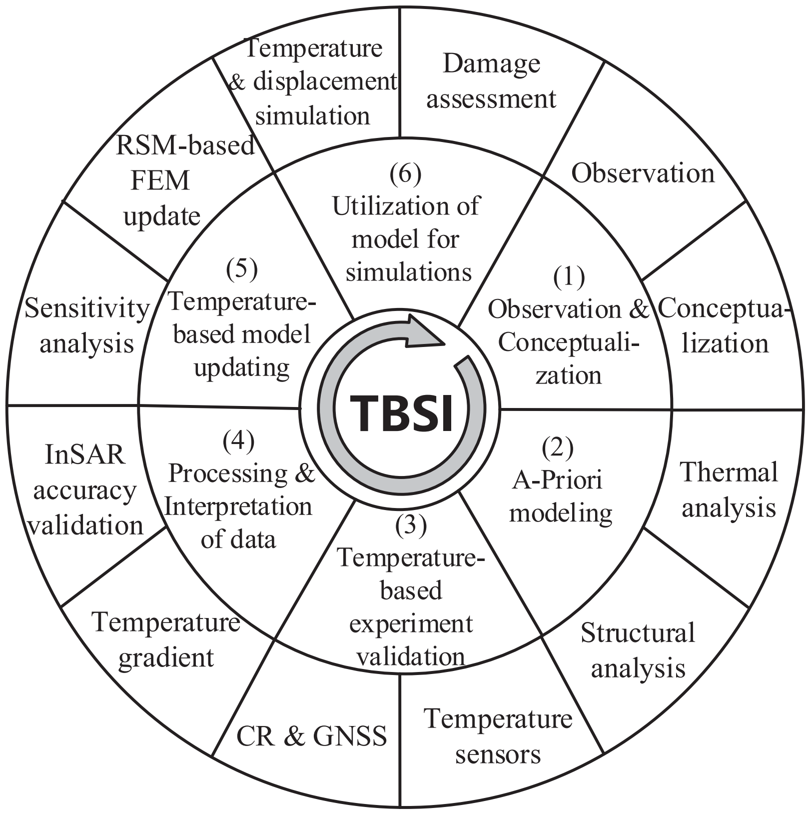

Figure 1. The six steps of TBSI.

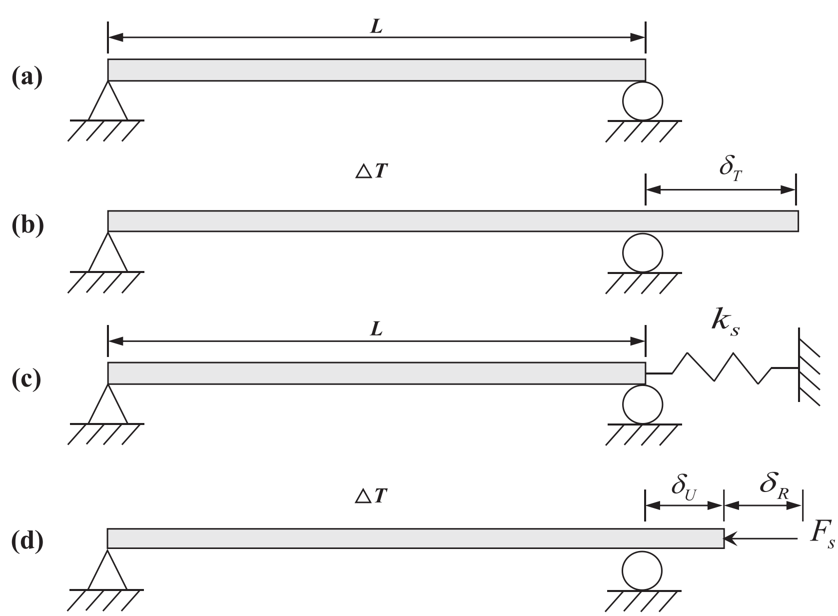

Figure 2. Simply supported beam under equivalent force substitution. (a) simply supported beam; (b) under uniform temperature change; (c) with longitudinal spring; (d) under equivalent spring force (shown in the negative direction).

using equation (2). The schematic diagram is shown in Figure 2(d).

$$\delta_R = \varepsilon_R L = \frac{F_S L}{AE} \tag{2}$$

In reality, for the simply supported beam with the action of the spring, the unconstrained deformation δ_U generates strain without stress, while the constrained deformation δ_R generates stress without strain. Therefore, the thermal stress generated in the simply supported beam with the spring under uniform temperature effect is given by equation (3), and the thermal deformation is given by equation (4).

$$\sigma_T = E\varepsilon_R = \frac{F_S}{A} \tag{3}$$

$$\delta_U = \delta_T - \delta_R = \alpha(\Delta T)L - \frac{F_S L}{AE} \tag{4}$$

The spring is a linear system, and the expression for the equivalent spring force is given by equation (5).

$$F_S = k_S \delta_U \tag{5}$$

Substituting equations (5) into (4) and simplifying yields:

$$\alpha = \frac{\left(\frac{AE}{L} + k_S\right) \cdot \delta_U}{AE(\Delta T)} \tag{6}$$

where, α on the left represents the "system", ΔT on the right represents the "input," and δ_U represents the "output." Given the "input" and "output," the "system" can be solved through reverse calculation. Naturally, the output is not confined to δ_U, other parameters in equation (6) may also be treated as outputs.

The theoretical framework above is based on the idealized assumption of a uniform temperature field. In practical engineering scenarios, indeterminate structures may exhibit non-uniform temperature distributions due to environmental factors (e.g., solar radiation gradients or partial shading), leading to combined axial and bending deformations. While the subsequent analysis accounts for temperature gradients induced by solar radiation, the explicit effects of shading are not included. Future work will extend the current theoretical framework to systematically quantify the impact of shading on damage diagnosis accuracy.

Sections *Theoretical fundamentals of InSAR technology* and *Theoretical foundation of bridge structural temperature field* will provide a detailed explanation of the displacement and temperature-related theories on the right-hand side of equation (6).

Theoretical fundamentals of InSAR technology

This study employs PSI method (Zhou Y et al., 2024) to obtain deformation information of bridges. PSI method enables the extraction of PS with stable backscatter characteristics from a series of SAR images, facilitating the inversion of the historical deformation sequence at the PS locations on the bridge.

Figure 3(a) shows the SAR observation geometry of the bridge, where point P represents the location of a PS point extracted from the bridge using PSI method. Since PSI method can only obtain line of sight (LOS) displacement between the satellite and the bridge, a 3D decomposition is required to obtain the true displacement of the bridge. Figure 3(b) presents the planar observation geometry of the bridge. The LOS displacement D_{LOS} of the bridge is the sum of the projections of its 3D displacement components along the LOS direction. The relationship between the LOS displacement D_{LOS} and the displacement components in each direction can be expressed with equation (7):

$$D_{LOS} = D_V \cos\theta + D_N \sin\theta \sin\gamma - D_E \sin\theta \cos\gamma \tag{7}$$

where, D_V, D_N, and D_E are the displacements in the vertical, north-south, and east-west directions, respectively, γ is the azimuth angle, and θ is the side-looking angle.

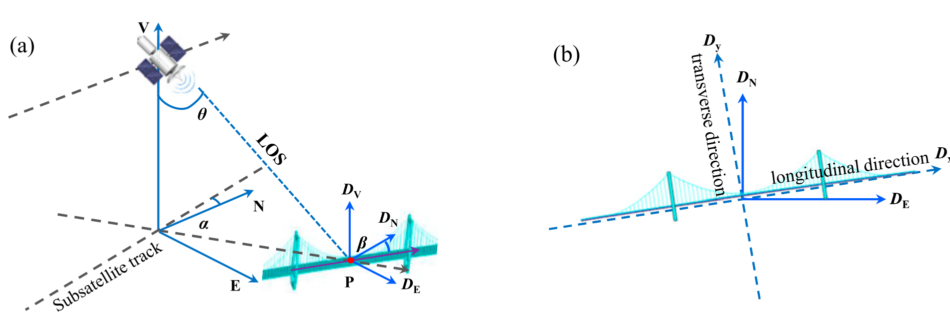

Figure 3. Satellite observation geometry. (a) SAR observation geometry of the target point; (b) Planar observation geometry of the bridge.

When the angle between the bridge and the north-south direction is denoted as β, the relationship between the north-south and east-west displacements of the bridge and its longitudinal D_x and transverse D_y displacements along the bridge is expressed in equation (8):

$$\begin{aligned} D_N &= D_y \sin\beta - D_x \cos\beta \\ D_E &= D_y \cos\beta + D_x \sin\beta \end{aligned} \tag{8}$$

By combining equations (7) and (8), the LOS displacement of the bridge can be expressed in terms of the longitudinal, transverse, and vertical displacements, as shown in equation (9):

$$\begin{aligned} D_{LOS} = D_V \cos\theta - D_x \sin\theta \cdot \sin(\gamma + \beta) \\ - D_y \sin\theta \cos(\gamma + \beta) \end{aligned} \tag{9}$$

Under the assumption that the longitudinal and transverse displacements are negligible, the relationship between the vertical displacement D_V and the LOS displacement can be expressed as follows:

$$D_V = \frac{D_{LOS}}{\cos\theta} \tag{10}$$

Theoretical foundation of bridge structural temperature field

For bridge structures, the heat transfer between the structure and the external environment is referred to as the bridge surface heat flux q, which consists of three components: heat convection q_c, thermal radiation from the surrounding environment q_r, and solar radiation q_s, with the latter two collectively referred to as thermal radiation.

Internal thermal conduction of bridge. By neglecting heat conduction along the bridge longitudinal direction, or simultaneously neglecting heat conduction in both longitudinal and transverse directions, the heat conduction process (Fourier and Gui, 1993) can be simplified for 2D or 1D analysis with specified initial and boundary conditions for solving corresponding partial differential equations. Currently, the boundary conditions for bridge structures are a combination of the second and third types of boundary conditions (Xu and Xia, 2011), as shown in equations (11) and (12):

$$\lambda \frac{\partial T_s}{\partial n} = h[T_a - T_s] + q_s \tag{11}$$

$$h = h_c + h_r \tag{12}$$

where, λ is the thermal conductivity of the target structure, assumed to be isotropic; n is the outward normal direction of the structure boundary; T_s is the structural temperature; T_a is the air temperature; q_s is the heat flux density on the external boundary; h is the overall heat transfer coefficient, comprising the convective heat transfer coefficient h_c and the radiative heat transfer coefficient h_r.

Thermal convection of bridge. Convective heat transfer occurs between the bridge structure and the surrounding environment, driven by the movement of fluid. The fundamental equation for convective heat transfer is given by equation (13) (Emanuel and Hulsey, 1978). The widely used empirical formula for calculating h_c is applied (Froli and Hariga, 1993), as shown in equation (14).

$$q_c = h_c s(T_s - T_a) \tag{13}$$

$$h_c = \begin{cases} 5.6 + 4v & v < 5m/s \\ 7.15v^{0.78} & v \geq 5m/s \end{cases} \tag{14}$$

where, s is the surface area; v is the wind speed.

Thermal radiation of bridge. The radiative heat transfer between the bridge structure and the surrounding air is shown in equation (15). The empirical formula proposed by Fernando is used to calculate h_r (Branco and Mendes, 1993), as shown in equation (16).

$$q_r = h_r\left({T_r}^4 - {T_s}^4\right) \tag{15}$$

$$h_r = \varepsilon[4.8 + 0.075(T_a - 5)] \tag{16}$$

where, T_r is the temperature of the external radiation source on the surface; ε is the emissivity of the structural material.

Solar radiation affects bridge temperature with direct, diffuse, and reflected components. This study obtains the radiation intensity using the empirical formula from the modified Kehlbeck model proposed by Elbadry and Ghali (1983), based on meteorological shared data (temperature, wind speed, and precipitation) from nearby weather stations. The radiative heat transfer caused by solar radiation is given by the following equation:

$$q_s = \alpha_m I \tag{17}$$

where, α_m is the absorptivity coefficient of the surface material; I is the total solar radiation intensity received by the structural surface.

Equation (17) is sensitive to cloudy, fog and darkness, and only applicable for calculating solar radiation intensity under clear weather conditions. Therefore, in this study, the temperature field of the bridge is only analyzed under clear weather conditions.

Equation (11) is further simplified, as shown in equation (18):

$$\lambda \frac{\partial T_s}{\partial n} = h[T_k - T_s] \tag{18}$$

$$T_k = T_a + \frac{\alpha_m I}{h} \tag{19}$$

where, T_k is the combined air temperature, accounting for ambient air temperature and solar radiation, and considered as the equivalent temperature of the external fluid acting on the structure.

MATLAB-ANSYS interface

In this study, MATLAB is used to efficiently interface with ANSYS to realize St-Id encompassing damage localization and quantification. The displacements under temperature effects are calculated in ANSYS and transferred to MATLAB, in which they are compared with the InSAR measured displacements utilizing the objective function. The thermal expansion coefficient α is adjusted to minimize the objective function, and the updated values are fed back into ANSYS. The interface between MATLAB and ANSYS integrates FE analysis with the DE algorithm, which relies on evolutionary processes and random search. This approach enhances simulation efficiency while leveraging MATLAB's data processing and visualization capabilities. The workflow of the ANSYS-MATLAB interface is illustrated in Figure 4.

The DE algorithm, introduced by Storn and Price (1997), is a population-based global optimization algorithm that generates new candidate solutions through differences between individuals. It uses mutation and crossover processes to iteratively approach the optimal solution. The DE algorithm provides a simple yet efficient approach for solving complex optimization problems in continuous spaces. Its basic steps include mutation, crossover, and selection. For each individual x_i in the population, the mutation process is shown in equation (20), where a new candidate solution (mutation vector) is generated by randomly selecting different individuals. The $v_i^{(g+1)}$ cannot be directly used as the new individual; it needs to undergo crossover with $x_i^{(g)}$ to combine new information while retaining features of the original individual. The crossover is performed using equation (21). Finally, the selection operation compares the objective function values of $u_i^{(g+1)}$ and $x_i^{(g)}$, retaining the individual with better fitness for the next generation. This operation is implemented through equation (22).

$$v_i^{(g+1)} = x_{r1}^{(g)} + F \cdot \left(x_{r2}^{(g)} - x_{r3}^{(g)}\right) \tag{20}$$

$$u_i^{(g+1)} = \begin{cases} v_i^{(g+1)} & if \;\; rand(j) \leq CR \, or \, j = j_{rand} \\ x_i^{(g)} & otherwise \end{cases} \tag{21}$$

$$x_i^{(g+1)} = \begin{cases} u_i^{(g+1)} & if \;\; f\left(u_i^{(g+1)}\right) \leq f\left(x_i^{(g)}\right) \\ x_i^{(g)} & otherwise \end{cases} \tag{22}$$

where, $v_i^{(g+1)}, u_i^{(g+1)}, x_i^{(g+1)}$ are the mutation, trial, and new solution vectors of the $i-th$ individual in the generation $g+1$, respectively. F is the differential weight. $x_{r1}^{(g)}$, $x_{r2}^{(g)}$, and

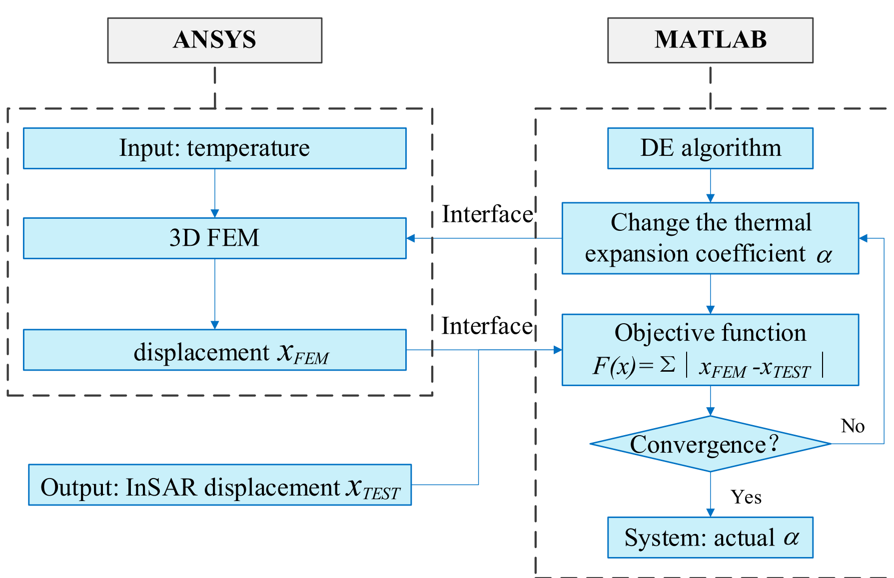

Figure 4. MATLAB-ANSYS interface.

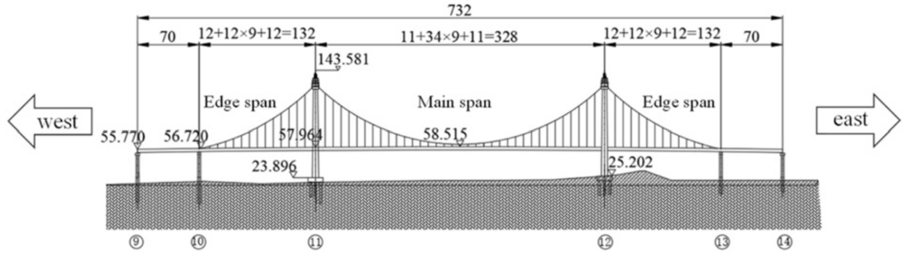

Figure 5. Elevation view. (unit: m).

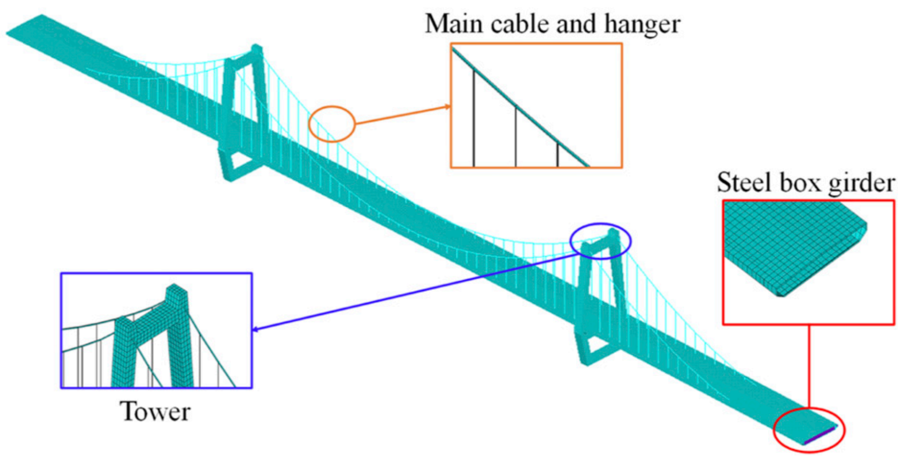

Figure 6. Prior 3D FEM.

$x_{r3}^{(g)}$ are three randomly selected distinct individuals from the current population. *CR* is the crossover probability, and *rand(j)* is a random number between 0 and 1. j_{rand} ensures that at least one dimension is inherited from the mutation vector. $f(\cdot)$ is the objective function.

Through this mechanism, the algorithm ensures that the overall fitness of the population improves in each generation and converge toward the optimal solution. The DE algorithm demonstrates strong global search capabilities, making it well-suited for complex problems, such as multi-degree-of-freedom systems. With minimal hyperparameter tuning, it is easy to implement and robust to environmental noise, converging to the optimal solution in fewer iterations.

TBSI of a long-span bridge

Step 1: Observation & conceptualization

The studied object is the Sanchaji Bridge in Changsha, Hunan, a self-anchored suspension bridge featuring twin towers and a 732 m long main bridge. The main girder has a width of 35 m and a height of 3.6 m. The orthotropic steel box girder is supported by two main cables, with a 25 m center-to-center distance between the cables and hangers. The bridge towers are reinforced concrete (RC) structures with a hollow box cross-section. Piers 9#-14# use bidirectional movable bearings combined with transverse limit bearings. In addition, the main bridge is connected to the east and west approach bridges by expansion joints. The elevation layout of the main bridge section is shown in Figure 5.

Table 2. Heat transfer analysis material parameters.

Parameter	Steel	Concrete	Asphalt
Density ρ (kg/m^3)	7850	2650	2365
Heat capacity c (J/kg·°C)	460	925	1075
Thermal conductivity k (W/m·°C)	60	2.71	1.8
Emissivity coefficient ε	0.8	0.88	0.92
Absorptivity coefficient α	0.685	0.65	0.90

Step 2: An a priori FE modeling

A prior FEM of the Sanchaji Bridge was established using ANSYS 18.0. This model aims to accurately simulate the temperature distribution of the bridge that can replace the previous simplified 2D or 3D sections. The complete 3D model, consisting of 24,964 elements and 30,129 nodes (Figure 6), was used for both heat transfer analysis and temperature-driven structural deformation analysis. The FEM for heat transfer includes thermal elements with boundary conditions: SHELL57 thermal shell elements for steel components (top plate with asphalt, bottom plate, web, and stiffeners), SOLID70 solid elements for tower columns, LINK33 bar elements for main cables and hangers, and MASS71 point elements for counterweights. The contact between the supports and the main beam is simulated using CONTA175 and TARGE170 elements. The connection between the main bridge and the east and west approach bridges is realized through vertical displacement constraints at the expansion joints. Material parameters are listed in Table 2.

In the structural analysis, 3D thermal elements were replaced by 3D structural elements in the FEM, while the configuration and meshing remained the same as in the thermal analysis. The temperature from the heat transfer analysis was automatically assigned on FEM nodes to obtain responses induced by temperature variations. A comparison of the element types used in the heat transfer and structural analyses is shown in Table 3.

Step3: Temperature-based experiment validation

To study the impact of temperature on the suspension bridge and verify the accuracy of the calculated temperature using meteorological data and displacement data from InSAR, a limited number of temperature sensors, strain sensors, artificial corner reflectors (CR), and Global Navigation Satellite System (GNSS) were installed on the bridge for verifying the TBSI theory, as shown in Figure 7(a). 18 artificial CRs were installed on the bridge deck between hanger spacings to intensify the bridge's scattering efficiency. The GNSS used for verifying the InSAR displacements was installed at the G02 and G03 sections. Temperature and strain sensors were installed at the G01 section of the edge span for the

Table 3. Correspondence between thermal elements and structural elements.

Analysis type	SHELL elements	SOLID elements	LINK elements	MASS elements	Contact elements
Heat transfer analysis	SHELL57	SOLID70	LINK33	MASS71	CONTA174 & TARGE169
Structural analysis	SHELL181	SOLID45	LINK180	MASS21	CONTA175 & TARGE170

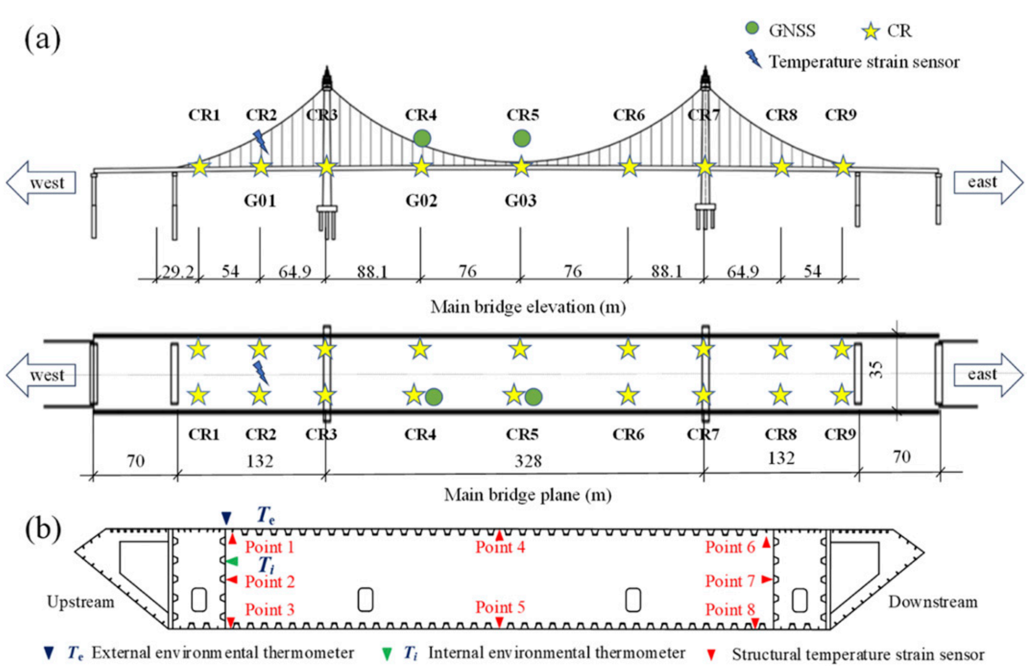

Figure 7. Sensor layout on the cross-section of the steel box girder section. (a) Layout of sensors, CR, and GNSS; (b) Layout of thermometers on beam section G01.

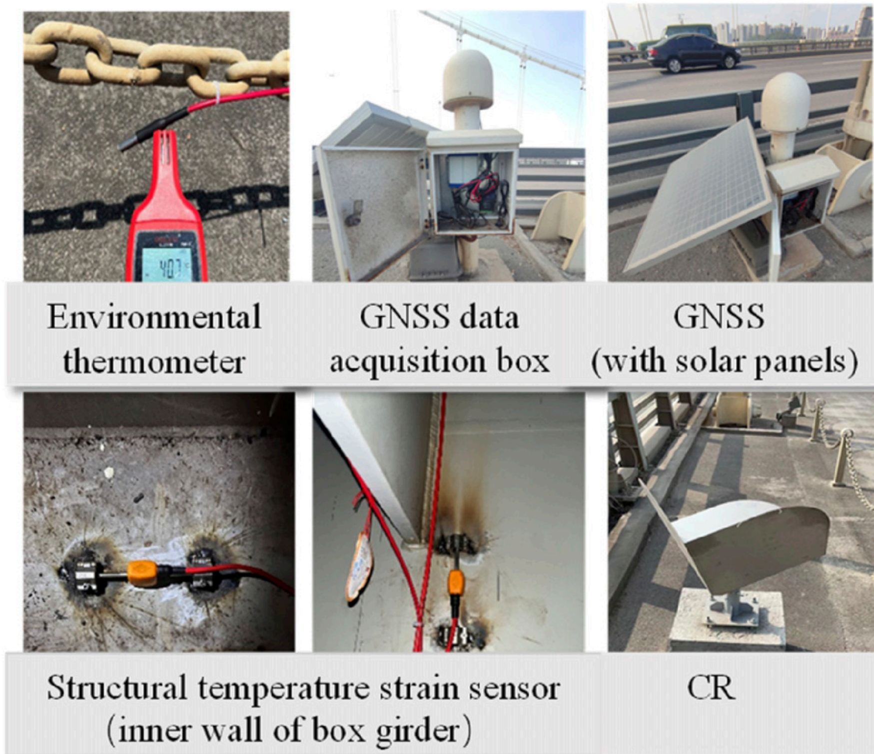

Figure 8. Actual layout of bridge sensors, GNSS, and CR.

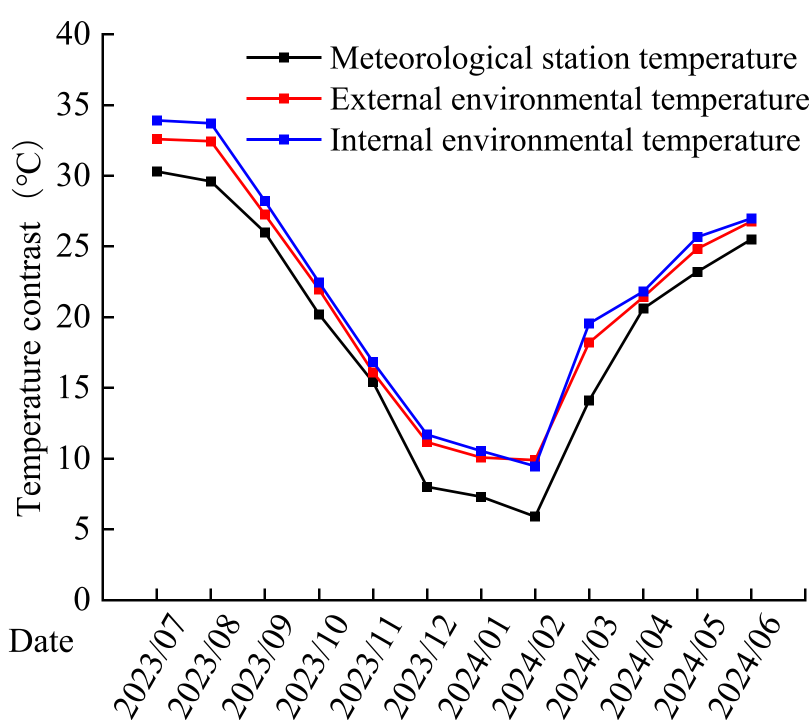

Figure 9. Monthly average temperature from July 2023 to June 2024.

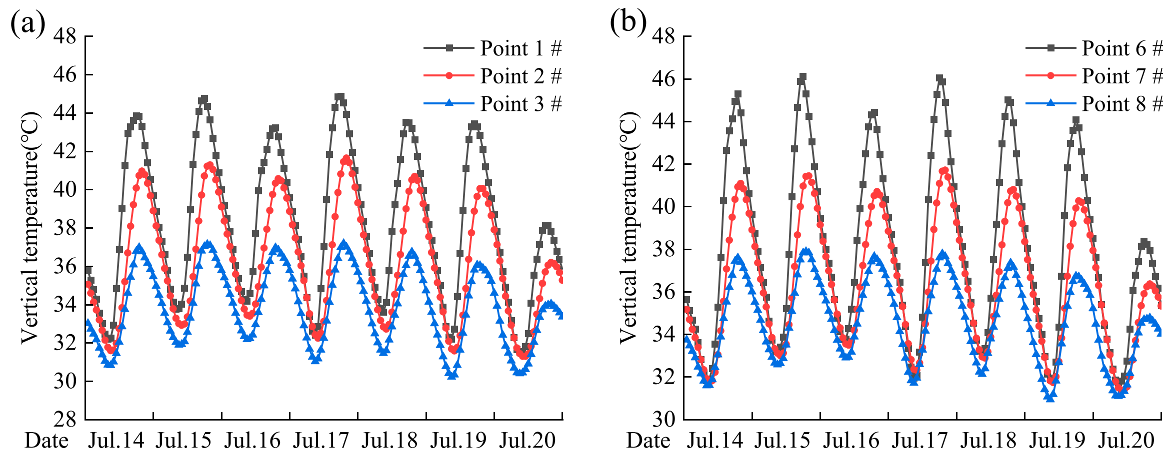

Figure 10. Vertical temperature distribution pattern of the G01 beam section. (a) Upstream; (b) Downstream.

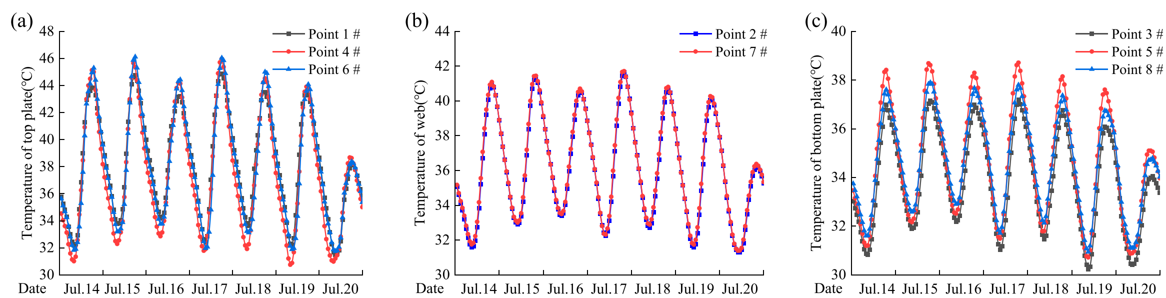

Figure 11. Transverse temperature distribution pattern of the G01 beam section. (a) Top plate; (b) Web; (c) Bottom plate.

comparison of TBSI theory (Figure 7(b)), with points 1-8 used to measure the structural temperature, validating the accuracy of temperature calculations based on meteorological data. T_i and T_e correspond to the internal and external ambient temperatures of the box girder, respectively. Measurements from these temperature and displacement sensors were taken every 30 minutes. The strain sensors were installed in July 2023, by which time the bridge had been in service for approximately 18 years. Therefore, the measured strain includes only elastic strain caused by live load and free thermal expansion strain caused by temperature changes, and the latter is removed by the thermal stress calculation (Jing et al., 2024). Figure 8 exhibits the detailed layouts of sensors and CRs on the bridge.

Step 4: Processing & interpretation of data

Temperature data of the Sanchaji bridge. Figure 9 compares the measured monthly average temperature of the bridge with meteorological data from July 2023 to July 2024. The measured temperature aligns well with the meteorological trend, although it is slightly elevated due to the urban heat island effect. The annual minimum temperature occurs in February, and the maximum occurs in July.

Temperature data from the G01 beam section, collected over seven consecutive days from July 14 to July 20, 2024, was analyzed to study the temperature distribution of the main girder. Figures 10 and 11 show the vertical and transverse temperature distributions of the G01 section, respectively. The analysis reveals that the temperature difference at the transverse measurement points is small, with the maximum difference being 2°C. However, the vertical measurement points exhibit a significant temperature gradient, which notably impacts the main girder structure and should be considered in subsequent analyses.

InSAR measured deflections and comparison with GNSS deformation. Since the installation of artificial CRs base in 2022, deformation data over 22 months was collected via the COSMO-SkyMed (CSK) satellite, covering the period from September 2022 to August 2024, with data missing for June 2024. Data is acquired monthly at approximately 6:00 a.m. Beijing time, and displacement values representing changes relative to the initial data acquisition time.

The LOS deformation velocity of the bridge's PS points is shown in Figure 12. The spatial distribution of PS points, based on CSK data, aligns well with the bridge's structure, and the maximum LOS displacement occurring near the expansion joints, which is consistent with the structural response of bridges subjected to temperature changes. The deformation velocity exhibits clear symmetry with respect to the center of the bridge. Figure 13 shows the LOS displacement from CR1 to CR9 on one side of the bridge, exhibiting a distinct sinusoidal trend. Since the CSK satellite data was acquired once a month, the role of temperature becomes dominant

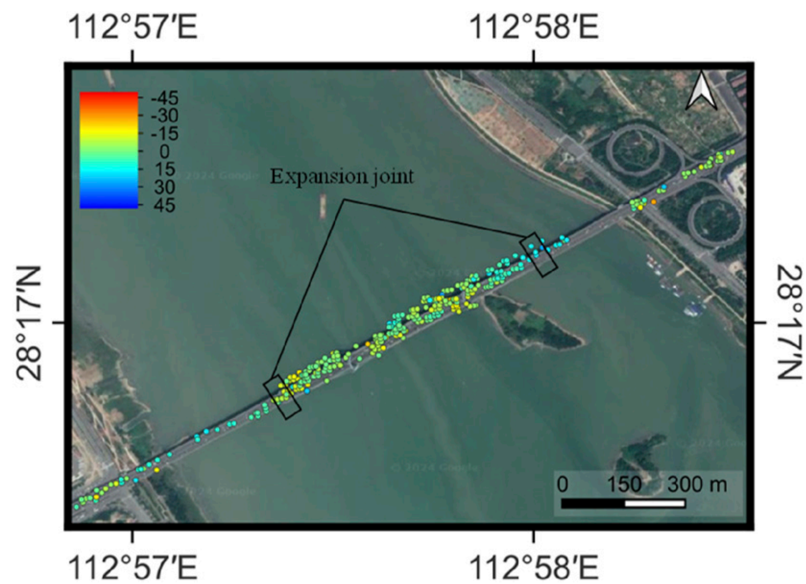

Figure 12. LOS deformation velocity of bridge PS points (mm/year).

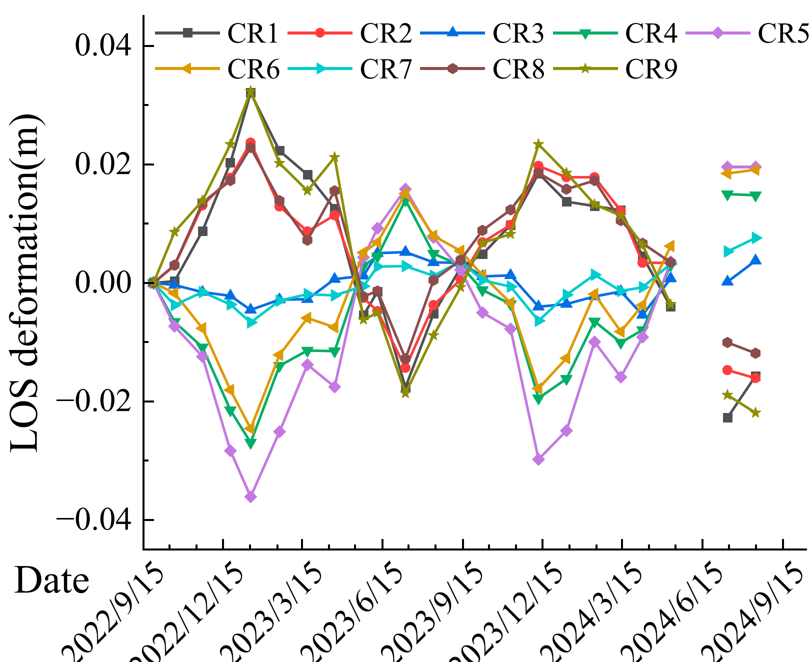

Figure 13. LOS displacement from CR1 to CR9.

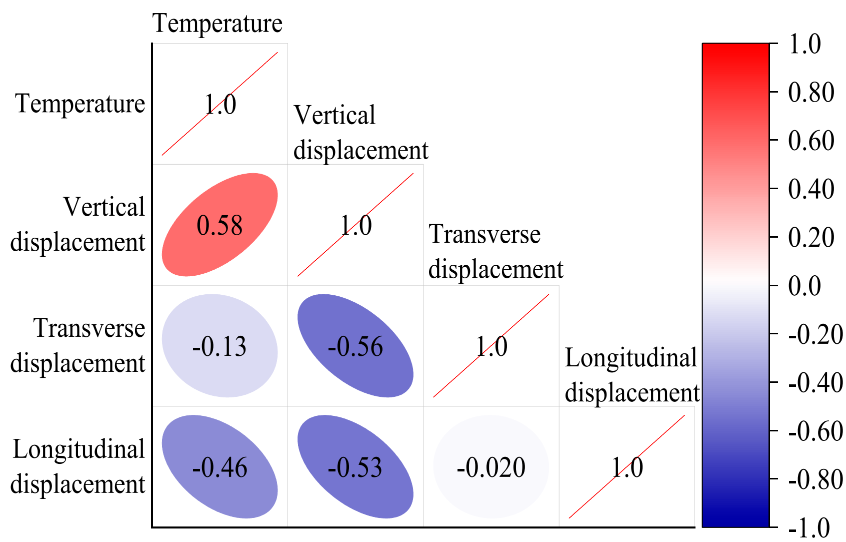

Figure 14. Correlation analysis between temperature and three-directional displacement.

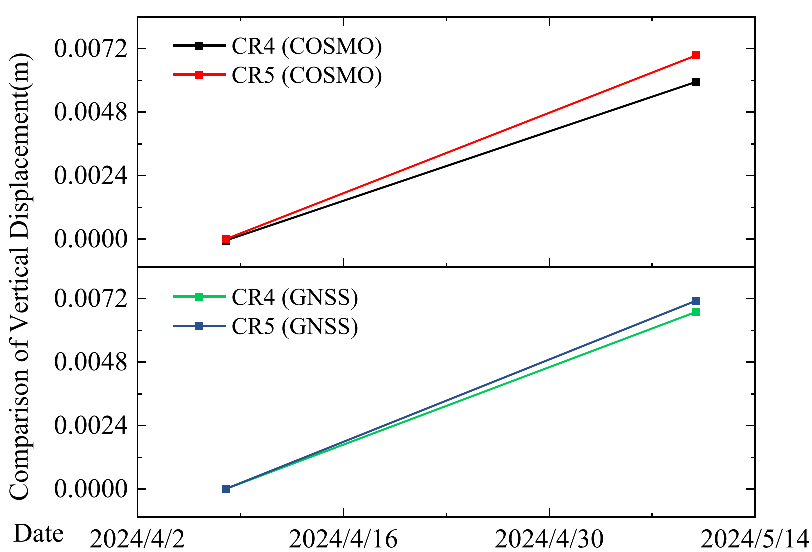

Figure 15. Comparison of CSK and GNSS vertical displacement data.

given its stability and prolonged impact on long-term displacement variations.

The GNSS system was installed in April 2024 to verify the accuracy of InSAR deformation data for the bridge. Before the verification, the displacement data in three directions (vertical, transverse, and longitudinal) from GNSS has been analyzed to identify the direction with the highest correlation to temperature, serving as the basis for comparison with CSK satellite data. The GNSS points are located at the G02 and G03 main span sections, as shown in Figure 7(a). The Pearson correlation (Pearson, 1897) between bridge temperature and displacements in three directions is shown in Figure 14. It can be observed that the vertical displacement has a strong positive correlation with temperature (correlation coefficient 0.58), while the transverse and longitudinal displacements show weak negative correlations (correlation coefficients −0.13 and −0.46, respectively). Therefore, the relationship between temperature and vertical displacement promises a more accurate basis for understanding the bridge's behavior and guiding design and maintenance.

For an equivalent comparison, the LOS displacement data from CSK satellites were decomposed using equation (10) to obtain vertical displacement data. This study compares the monthly average of the GNSS data with the CSK satellite data collected during April and May 2024, as shown in Figure 15. At CR4 and CR5, the directions of vertical displacement for both GNSS and CSK are coincident. The discrepancy is subtle, within 2 mm, suggesting that CSK data can provide precise measurements of bridge displacement.

Step 5: Temperature-based model updating

The prior FEM is updated based on the temperature and temperature-driven response data collected and processed in step 4. This study applies a Response Surface Method (RSM) (Ren and Chen, 2010) to determine the relationship between structural responses and input variables through optimization and to ultimately obtain a RS model that represent actual structural characteristics. The objective function is the sum of squared relative errors between the simulated and measured values:

$$\min f(a) = \sum_{i=1}^{k} \left(1 - \frac{R_{fi}}{R_{ti}}\right)^2 \tag{23}$$

where, R_{fi} (i = 1, 2, ⋯, k) is the simulated response (displacement or strain) value, and R_{ti} is the measured value at section i point.

The complete RSM modification process generally consists of four steps: parameter screening, significance testing, response surface function fitting, model validation, and optimization. In this study, based on considerations of research focus and manuscript length constraints, we emphasize two core components: screening of parameters requiring correction and model validation. The omitted parameter significance testing step ensures model correction efficiency, and the response surface fitting process significantly reduces computational costs for parameter optimization.

Based on engineering experience and practical considerations, the elastic modulus E and density ρ of the cables, towers, and main beam are selected as key parameters. A sensitivity analysis is conducted to eliminate those with minimal impact on the results of equation (23). Considering the fact that only data from sensors on the main beam sections are utilized for validation, the strain at the top plate, web, and bottom plate of the G01 section and displacement at G03 are selected as target values for correction. Assuming that the parameters of the initial FEM (i.e., ρ and E) are set to 1, the standardized parameter is defined as the ratio of the modified parameters to its initial values. Figure 16 indicates that the objective function is highly sensitive to the main beam's ρ and E while less sensitive to corresponding parameters of the main cable

Table 4. Comparison before and after parameter correction.

Parameter	E of top plate (GPa)	E of bottom plate (GPa)	E of web plate (GPa)	ρ (kg/m^3)
Before correction	206	206	206	7850
After correction	229.7	181.3	197.4	8698.4
Relative error (%)	11.5%	−11.9%	−4.1%	10.8%

Table 5. Comparison before and after model modification.

Parameter	Point 4 strain (με)	Point 2 strain (με)	Point 5 strain (με)	G03 Displacement (mm)
Measured value	−10.2	−49.8	68.6	6.08
Before correction	−14.6	−58.7	92.7	6.93
After correction	−10.7	−53.8	81.2	6.89
Relative error (%)	4.7%	8.0%	18.3%	13.3%

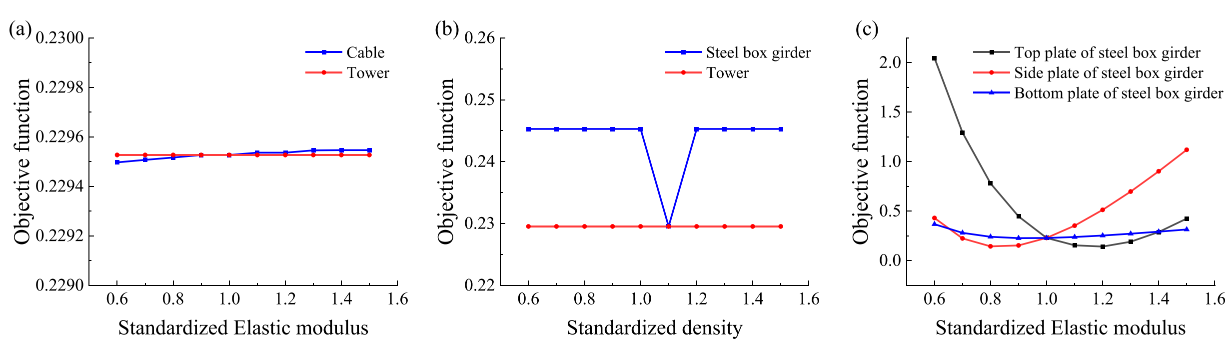

Figure 16. Sensitivity analysis curves: (a) Elastic modulus of main cable and bridge tower; (b) Density of main beam and bridge tower; (c) Elastic modulus of main beam.

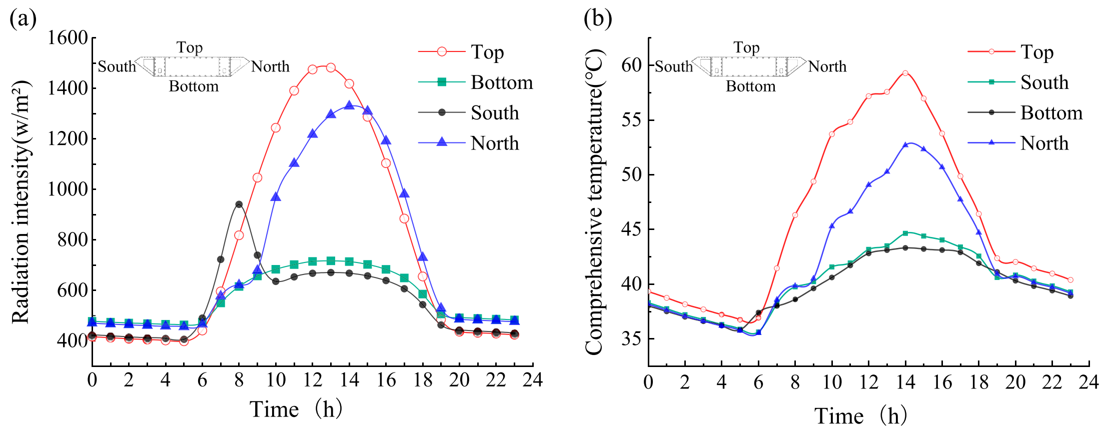

Figure 17. July 15, 2024. (a) Total solar radiation intensity; (b) Combined temperature.

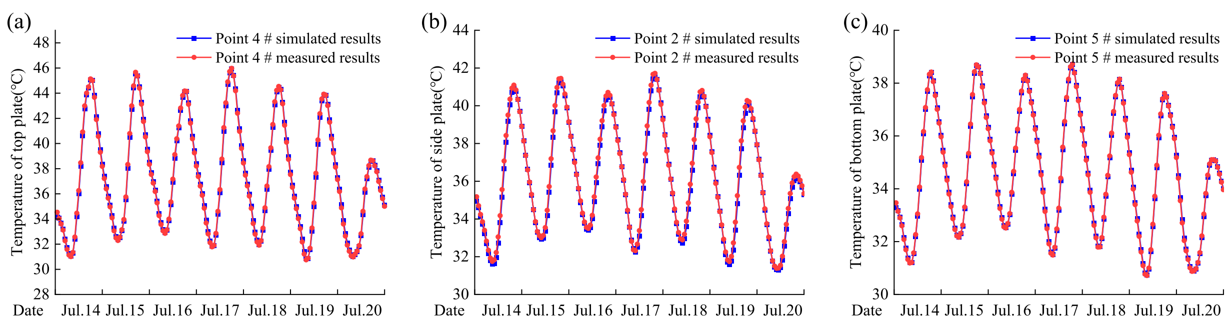

Figure 18. Comparison of measured and simulated temperatures. (a) Top plate; (b) Web plate; (c) Bottom plate.

and bridge tower. Therefore, the critical parameters for model updating are the ρ and E of the steel box girder.

Data from a sunny afternoon at 4:00 p.m. was randomly selected for correction, as the peak of solar radiation usually occurs at this time, resulting in the maximum strain induced by temperature effects. Tables 4 and 5 show the comparison of the main beam's ρ and E before and after correction, along with the measured and calculated values. After correction, E of the top plate increased due to the combined treatment of the asphalt concrete layer and top plate, while the bottom plate and web showed stiffness degradation over time.

Step 6: Utilization of model for simulations

Temperature distribution simulation. A heat transfer analysis was conducted for the bridge using equations (18) and (19). Since no anemometers and pyranometer data were available on the bridge, data from the nearest meteorological station (located less than 20 km away) was adopted for calculations to ensure accuracy, as suggested in reference (Sadhu et al., 2017). The weather data from the nearest meteorological station located 9.91 km from the bridge and obtained from the Meteostat platform (https://meteostat.net/en/) was utilized in this study. The total radiation intensity I for selected summer days is calculated, as shown in Figure 17(a).

Table 6. MAEs and RMSEs of simulated versus measured bridge temperatures in summer (Unit: °C).

Evaluation metrics	Top plate	Web plate	Bottom plate
MAE	0.155	0.151	0.056
RMSE	0.173	0.196	0.063

On July 15, 2024, the sunrise and sunset times were 5:41 a.m. and 7:26 p.m., respectively. As shown in Figure 17(a), from sunrise to 8:51 a.m., the south side of the components was exposed to direct solar radiation, with a calculated maximum I of 14.82 MJ/m^2, closely matching the measured value of 14.69 MJ/m^2 in the bridge's location. Based on equation (19), heat transfer analysis for the suspension bridge requires boundary conditions. The combined temperature T_k was obtained on July 15th, as shown in Figure 17(b).

Due to different I on four surfaces of the bridge, the highest T_k occurred on the bridge deck, while the lowest on the bottom surface. The north-facing surface experienced a

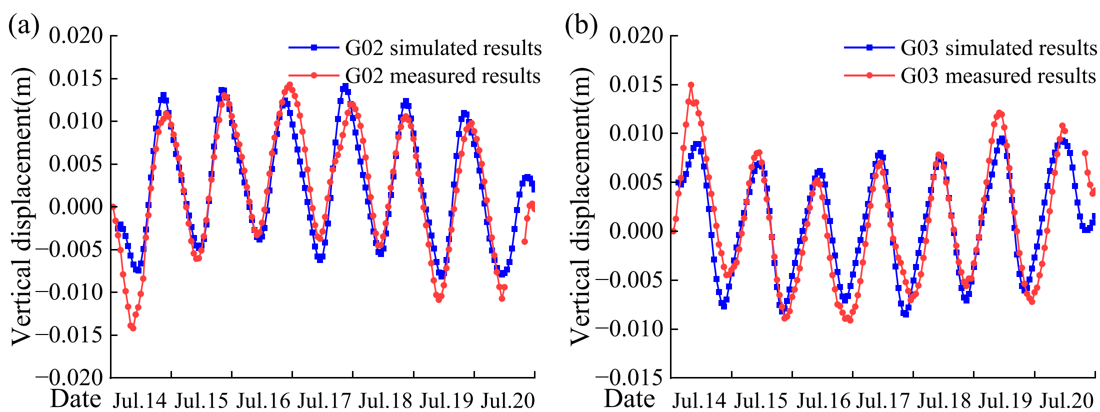

Figure 19. GNSS measured displacement versus simulated displacement. (a) G02; (b) G03.

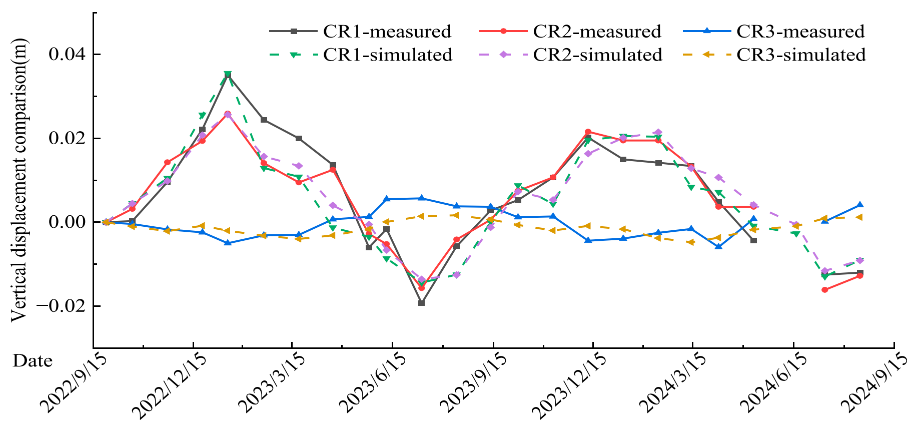

Figure 20. Comparison of measured and simulated vertical displacements for CR1-CR3.

higher temperature than the south-facing surface because the Sanchaji Bridge is angled at 32°31′ to east, so the north-facing surface receives significantly more solar radiation.

Three representative points on the G01 section (top plate, bottom plate, and web plate) were selected for comparison between measured summer temperatures (July 14th to 20th) and FEM simulations based on the global bridge numerical model, as shown in Figure 18. The results show high consistency, validating both the temperature calculation method and the effectiveness of the FE heat transfer analysis.

The differences between measured data and simulation results were evaluated by calculating the Mean Absolute Error (MAE) and Root Mean Square Error (RMSE) (equations (24) and (25)). The errors between simulated and measured temperature values are summarized in Table 6.

$$\mathrm{MAE} = \sum\nolimits_{i=1}^{n} |N_i - M_i| \Big/ n \tag{24}$$

Table 7. MAEs and RMSEs between simulated and measured bridge displacements (units: mm).

Evaluation metrics	G02 and G03 (GNSS)	CR1~CR3 (CR)
MAE	2.19	3.25
RMSE	2.71	4.31

$$\mathrm{RMSE} = \sqrt{\sum\nolimits_{i=1}^{n} (N_i - M_i)^2 \Big/ n} \tag{25}$$

where N_i is the measured value, M_i is the simulated value, and n is the total sample size.

Smaller MAE and RMSE values indicate better agreement between simulated and measured results, demonstrating higher computational accuracy. Table 6 shows strong consistency between observed and simulated summer temperatures, which confirms the reliability of the meteorological-data-driven method for bridge

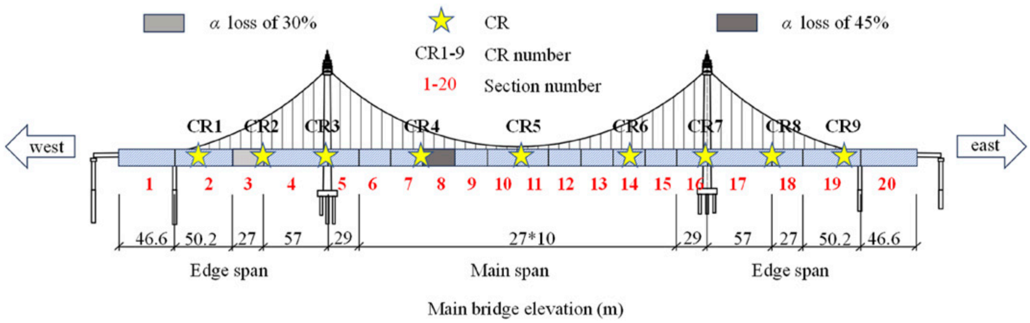

Figure 21. Bridge section division and damage area schematic (unit: m).

thermal analysis and further supports the FEM's capability in heat transfer simulations.

Temperature response simulation. The temperature response study of the suspension bridge employs the same element meshing as in the Section 3.6.1. The comparison of simulated and measured temperature responses covers the same period as in the previous section, from July 14th to July 20th, as shown in Figure 19. Furthermore, the displacement results for each subsequent day are presented relative to the first day's initial time.

Figure 19 compares the vertical measured and simulated displacements at main span sections G02 and G03 relative to the initial time, showing consistent trends with periodic fluctuations. Deviations on certain days (e.g., Day 1 and Day 4) might be owing to environmental factors like wind speed or solar radiation fluctuations, which are not included in the simplified temperature gradient treatment of the model.

According to the correlation analysis in section 3.4.2, the vertical displacement has the closest relationship with temperature. Therefore, the LOS displacement of the bridge was decomposed using equation (10), with γ set to 168°, θ to 24°, and β to 31°. Figure 20 shows the comparison between the simulated vertical displacement results and the measured values for CR1-CR3 obtained from the decomposition.

The errors in Figures 19 and 20 were quantified using equations (24) and (25), with detailed results presented in Table 7. The results indicate that the errors between the measured and simulated values are close to zero. The structural field analysis of the FEM aligns with the actual results, showing identical timing and magnitude of peaks. The maximum deviation does not exceed 3.5 mm, further validating the accuracy of the FEM in structural response analysis.

Verification of TBSI based on the DE algorithm. This section verifies the possibility of using TBSI theory to locate and quantify the damage and its locations in bridge structures. The updated model is input with T_k data from SAR satellite imaging (Sept 2022–Aug 2023), covering various seasonal and climatic conditions, offering a more accurate reflection of the bridge's stress state than a single temperature input. Damage is applied to specific sections, with measured displacements used as output. Using MATLAB-ANSYS application programming interface (API) algorithm, the optimal solution for thermal expansion coefficient of all regions is estimated, minimizing the error between simulated thermal deformation and measured values. Conventional damage does not alter the material's inherent α. Therefore, an equivalent thermal expansion coefficient, denoted as α_{eff} (equation (26)), is defined to characterize thermodynamic behavior anomalies caused by structural damage. When bridge structures undergo stiffness degradation (e.g., cracks, corrosion), constraint failure (e.g., bearing seizure), or geometric discontinuities (e.g., debonding), the thermal displacement response ($\delta_{damaged}$) deviates from the theoretical value of the healthy state ($\delta_{healthy}$), resulting in α_{eff} significantly diverging from the material's α value. The error function is defined as equation (27). Therefore, the FEM damage parameter identification is transformed into solving the optimization problem defined by equation (28).

$$\alpha_{eff} = \frac{\delta_{damaged}}{\delta_{healthy}} \cdot \alpha \tag{26}$$

$$f\left(\alpha_{eff}\right) = \sum\nolimits_{i=1}^{k} \left| R_{fi} - R_{ti} \right| \tag{27}$$

$$\begin{cases} minf\left(\alpha_{eff}\right) \\ s.t. \ \ \alpha_l \le \alpha_{eff} \le \alpha_u \end{cases} \tag{28}$$

where, $\delta_{damaged}$ and $\delta_{healthy}$ represent the displacements in the damaged and healthy states, respectively. R_{fi} $(i = 1, 2, \cdots, k)$ is the simulated response value and R_{ti} is the measured value at section i point. α_l and α_u are the lower and upper bounds of the parameter to be corrected, respectively.

The ratio of the α_{eff} of each section during the iteration process to the initial design state α_{eff} is defined as the normalized thermal expansion coefficient α_s. The main span

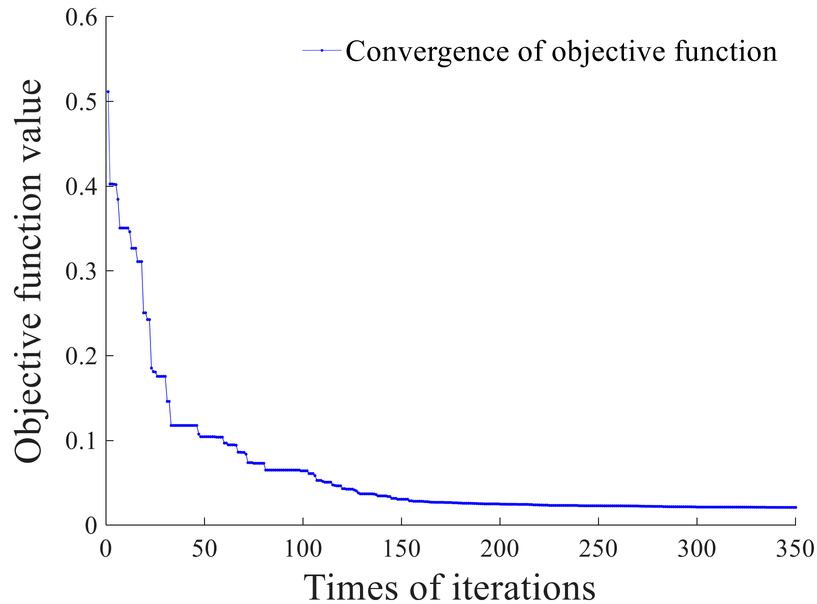

Figure 22. Iteration process of damage identification.

and edge spans of the bridge are divided into 20 sections, as shown in Figure 21, with artificially hypothesized damaged areas marked in the figure. I(t) is assumed that the equivalent thermal expansion coefficient α_{eff} of section 3 in the edge span is damaged by 30% and that of section 8 in the main span is damaged by 45%, with sections 3 and 8 located near CR2 and CR4, respectively. The DE algorithm is used to identify the location and extent of the damage.

The DE algorithm's initial population size is set to 10, with a weight F of 0.8 and a CR of 0.8. MATLAB and ANSYS interacted for 350 iterations, and the results gradually converged, as illustrated in Figure 22. The detailed algorithmic procedure is summarized in Algorithm 1. In this process, x represents the number of α_{eff} values to be identified, N is the total number of DE iterations, *pop_size* is the population size in each generation, and [*lb*, *ub*] denote the lower and upper bounds of α_{eff} Values. Figure 22 shows the iteration convergence, with a rapid decrease in the objective function during the first 150 iterations. As the number of iterations increases, the rate slows and the function stabilizes, indicating the effectiveness of the optimization. The objective function converges to around 0.0209, with the absolute difference between measured and simulated values at the 20 points approaching zero, indicating the accurate identification of the damage location and extent. Table 8 shows the final results after the model converges, and Figure 23 visualizes the identification results.

Table 8 and Figure 23 demonstrate that the DE algorithm, combined with temperature and displacement data for inverse analysis, can effectively locate the α damage areas. Sections 3 and 8 have significantly lower values of α_{eff} compared to the other sections, indicating considerable damage in these sections. The α_s values for these sections are 0.7 and 0.55, and the identified results are 0.7222 and 0.5417, with errors of 3.17%, and −1.51%, respectively, which are within an acceptable range. Errors in other sections are generally small, suggesting light or no noticeable damage, with most errors within 8% (Table 8).

Table 8. Damage identification results for each section.

Section number	α_s	Identification result	Relative error (%)
1	1	1.0000	0.00
2	1	0.9990	−0.10
3	0.7	0.7222	3.17
4	1	1.0000	0.00
5	1	1.0000	0.00
6	1	0.9291	−7.09
7	1	0.9972	−0.28
8	0.55	0.5417	−1.51
9	1	0.9931	−0.69
10	1	1.0000	0.00
11	1	1.0000	0.00
12	1	1.0000	0.00
13	1	0.9994	−0.06
14	1	1.0000	0.00
15	1	0.9918	−0.82
16	1	0.9332	−6.68
17	1	0.9999	−0.01
18	1	0.9642	−3.58
19	1	0.9251	−7.49
20	1	0.9894	−1.06

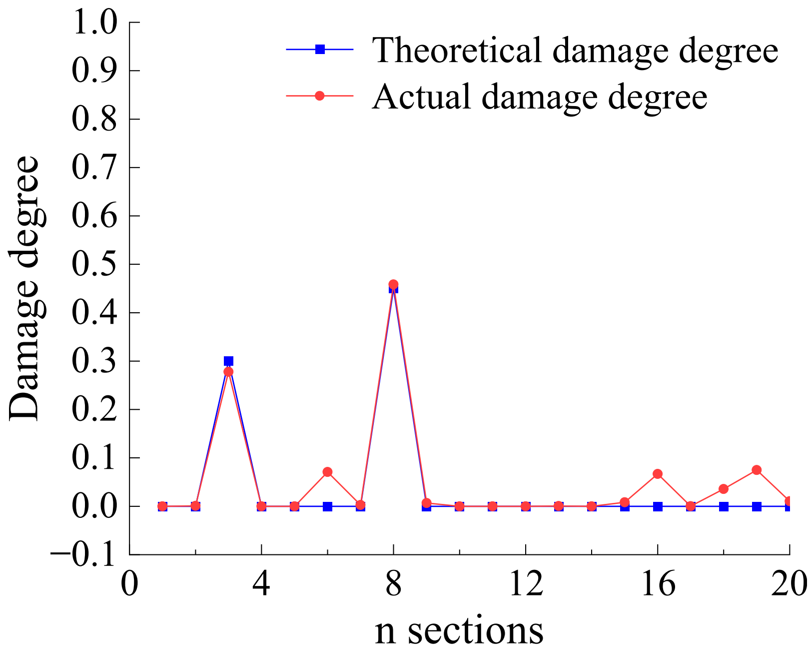

Figure 23. Damage identification results for sections 3 and 8.

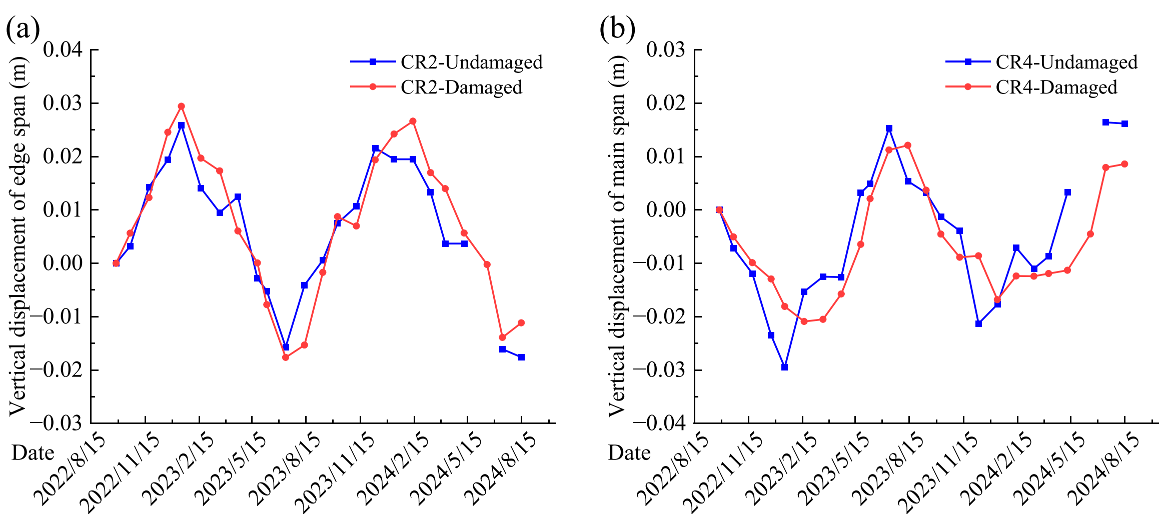

Figure 24. Damage-induced vertical displacement comparison. (a) edge span; (b) main span.

Algorithm 1 MATLAB-ANSYS Interface via Differential Evolution (DE)

Input: *x*, *N*, *pop_size*, *[lb, ub]*, *F*, *CR*, *InSAR_data*, *ANSYS_config*
Output: *best_solution* as the identified α_{eff} values
Initialization: *population* ← random(*pop_size, x*) within *[lb, ub]*; *best_objective* ← ∞
For ***iter*** **= 1 to** ***N*****:**
  For ***i*** **= 1 to** ***pop_size*****:**
    objective[i] ← ComputeObjective(*population[i]*, *InSAR _data*, *ANSYS_config*)
  best_solution ← individual with min(*objective*)
  For ***i*** **= 1 to** ***pop_size*****:**
    Select distinct indices *r1, r2, r3 (≠ i)*;
    mutant ← clip(*population[r1] + F*(population[r2] - population[r3])*, *lb*, *ub*);
    trial ← Crossover(*population[i]*, *mutant*, *CR*);
    trial_objective ← ComputeObjective(*trial*, *InSAR _data*, *ANSYS_config*);
    If *trial_objective* < *objective[i]* **then** *population[i]* ← *trial*
Return: *best_solution*

By substituting the identified parameters α_{eff} into the FEM, the vertical displacements of the main and edge spans were calculated and compared with CSK satellite data, as shown in Figure 24. Since sections 3 and 8 are located near CR2 and CR4, respectively, displacement comparisons before and after damage at these locations are presented. The results indicate that the 45% damage near CR4 significantly reduces the deformation ability of the bridge under temperature changes, leading to a smaller displacement compared to the undamaged state. In contrast, due to the relatively small deformation in the main span of the bridge, the edge span at CR2 experiences larger displacement than in the undamaged condition. Overall, the displacement differences in the damaged sections are evident, confirming the impact of damage on the structure.

Conclusions

In this paper, the TBSI method is introduced to perform damage assessment of bridges using InSAR technology, providing a lightweight solution that overcomes the limitation of using InSAR-derived deformation data for structural condition evaluation. This method uses temperature as input and displacement as output to identify regions with abnormal thermal expansion coefficients. The FEM of a bridge is established for thermal-structural coupling analysis, and model updates are implemented through sensitivity analysis. Based on the above work, specific conclusions could be drawn as follows:

(1) A MATLAB-ANSYS interface programming algorithm along with the approach of St-Id inverse problems was utilized to overcome the challenges of using InSAR technology for damage assessment of bridges. Temperature data obtained from meteorological shared data and heat transfer analysis were used as input, while displacement measurements from InSAR technology serve as output to identify the thermal expansion coefficient α of the bridge system, facilitating the damage assessment of bridges.

(2) The structural temperature of the Sanchaji Bridge was calculated using data from the nearest meteorological station (such as temperature, wind speed, and solar radiation intensity). Thermal-structural coupling analysis was performed using ANSYS software to obtain the temperature field and structural response (e.g., displacement) of the bridge. During this process, the thermal elements were converted to structural elements without the need for remeshing, improving analysis efficiency.

(3) The vertical displacements, obtained by decomposing the LOS displacement data from the CSK satellite, were compared to GNSS measurements. The directions of displacement are consistent, with only subtle variations, and the discrepancy between them does not exceed 2 mm. This further validates the capability of InSAR data for measuring displacement and confirms its accuracy. The simulated and measured vertical displacement results for CR1-CR3 show strong agreement, with closely matching peak times and magnitudes.

(4) Assuming damage occurs in two regions of the bridge structure, the DE algorithm converges effectively, precisely locating the damage areas and quantifying the damage levels. For long-span suspension bridges, the identification deviation does not exceed 8%, with errors within an acceptable range, demonstrating the method's feasibility and accuracy.

Declaration of conflicting interests

The author(s) declared no potential conflicts of interest with respect to the research, authorship, and/or publication of this article.

Funding

The author(s) disclosed receipt of the following financial support for the research, authorship, and/or publication of this article: The authors sincerely appreciate the funding support provided by the National Natural Science Foundation of China (NSFC) (No.52278306), the Key Research and Development Program of Hunan Province (No.2022SK2096), the Hunan Provincial Natural Science Foundation of China (No. 2023JJ70003), the National Natural Science Foundation of China (No. 52408327), the Natural Science Foundation of Hunan Province, China (No. 2024JJ6198). The meteorological station data was downloaded from platform Meteostat.

ORCID iDs

Xiaowan Xu https://orcid.org/0009-0003-1536-3736
Guanwang Hao https://orcid.org/0000-0002-3463-9625

References

Bacinskas D, Kamaitis Z, Jatulis D, et al. (2013) Load testing and model updating of a single span composite steel-concrete railway bridge. *Procedia Engineering* 57: 127–135.

Barr PJ, Eberhard MO and Stanton JF (2001) Live-load distribution factors in prestressed concrete girder bridges. *Journal of Bridge Engineering* 6(5): 298–306.

Bell ES, Lefebvre PJ, Sanayei M, et al. (2013) Objective load rating of a steel-girder bridge using structural modeling and health monitoring. *Journal of Structural Engineering* 139(10): 1771–1779.

Branco FA and Mendes PA (1993) Thermal actions for concrete bridge design. *Journal of Structural Engineering* 119(8): 2313–2331.

Breña SF, Jeffrey AE and Civjan SA (2013) Evaluation of a noncomposite steel girder bridge through live-load field testing. *Journal of Bridge Engineering* 18(7): 690–699.

Cai J, Wu ZS and Li ZX (2004) Statistical approach to evaluating the status of an existing structure using static test data. *Engineering Mechanics* 21(6): 76–83.

Caspani VF, Tonelli D, Rocca A, et al. (2023) Satellite InSAR technology for structural health monitoring of road bridges and the surrounding territory: a case study. In: Sensors and smart structures technologies for civil, mechanical, and aerospace systems 2023, California, *United States*, 12-17 March 2023, 293–302.

Catbas FN, Moon F and Aktan AE (2010) An integrated view for structural identification of civil infrastructure systems: an overview of a collaborative ASCE committee effort. In: Structures congress 2010, Orlando, FL, 12–15 May 2010, 440–446.

Chajes MJ and Shenton HW III (2006) Using diagnostic load tests for accurate load rating of typical bridges. *Bridge Structures* 2(1): 13–23.

Chen ZS, Zhou X, Wang X, et al. (2017) Deployment of a smart structural health monitoring system for long-span arch bridges: a review and a case study. *Sensors* 17(9): 2151.

Cho K and Cho J-R (2022) Effect of temperature on the modal variability in short-span concrete bridges. *Applied Sciences* 12(19): 9757.

Dilger WH, Ghali A, Chan M, et al. (1983) Temperature stresses in composite box girder bridges. *Journal of Structural Engineering* 109(6): 1460–1478.

Elbadry MM and Ghali A (1983) Temperature variations in concrete bridges. *Journal of Structural Engineering* 109(10): 2355–2374.

Emanuel JH and Hulsey JL (1978) Temperature distributions in composite bridges. *Journal of the Structural Division* 104(1): 65–78.

Farneti E, Cavalagli N, Venanzi I, et al. (2023) Residual service life prediction for bridges undergoing slow landslide-induced movements combining satellite radar interferometry and numerical collapse simulation. *Engineering Structures* 293: 116628.

Fourier J and Gui Z (1993) *Analytical Theory of Heat*. Wuhan, China: Wuhan Publishing House.

Froli M and Hariga N (1993) La risposta termica per effetti ambientali dei ponti a travata in ca, cap. *Atti delle Giornate AICAP* 93: 161–170.

Han QH, Ma Q and Xu J (2021a) Temperature-driven damage identification method based on cuckoo search. *Journal of Building Structures* 42: 473–480.

Han QH, Ma Q, Xu J, et al. (2021b) Structural health monitoring research under varying temperature condition: a review. *Journal of Civil Structural Health Monitoring* 11: 149–173.

Huang QH, Crosetto M, Monserrat O, et al. (2017) Displacement monitoring and modelling of a high-speed railway bridge using C-band Sentinel-1 data. *ISPRS Journal of Photogrammetry and Remote Sensing* 128: 204–211.

James ED (2016) *Development of a Rapid Field Evaluation Method for Steel Girder Bridges*. Cookeville, Tennessee: Tennessee Technological University.

James ED and Yarnold MT (2017) Rapid evaluation of a steel girder bridge: case study. *Journal of Bridge Engineering* 22(12): 05017013.

Jing Q, Shan YS, Zhang L, et al. (2024) Typhoon-and temperature-induced responses of a cable-stayed bridge. *Advances in Structural Engineering* 27(16): 2773–2789.

Kourehli SS, Bagheri A, Amiri GG, et al. (2013) Structural damage detection using incomplete modal data and incomplete static response. *KSCE Journal of Civil Engineering* 17: 216–223.

Kromanis R and Kripakaran P (2016) SHM of bridges: characterising thermal response and detecting anomaly events using a temperature-based measurement interpretation approach. *Journal of Civil Structural Health Monitoring* 6: 237–254.

Li LF, Chen B, Zhou LR, et al.. (2023) Thermal behaviors of bridges — A literature review. *Advances in Structural Engineering* 26(6): 985–1010.

MOTOC (2024) 2023 statistical bulletin on the development of the transportation Industry. *China Communications News* 002: 1–12.

Murphy B and Yarnold M (2018) Temperature-driven structural identification of a steel girder bridge with an integral abutment. *Engineering Structures* 155: 209–221.

Pearson K (1897) Mathematical contributions to the theory of evolution.—on a form of spurious correlation which may arise when indices are used in the measurement of organs. *Proceedings of the Royal Society of London* 60(359-367): 489–498.

Qin SQ, Zhang YZ, Zhou YL, et al. (2018a) Dynamic model updating for bridge structures using the kriging model and PSO algorithm ensemble with higher vibration modes. *Sensors* 18(6): 1879.

Qin XQ, Ding XL and Liao MS (2018b) Capturing the deformation characteristics of cable-stayed bridges with multi-temporal SAR interferometry. In: 2018 fifth international workshop on earth observation and remote sensing applications (EORSA), Xi'an, China, 18-20 June 2018, 1–5.

Rainieri C and Fabbrocino G (2015) Development and validation of an automated operational modal analysis algorithm for vibration-based monitoring and tensile load estimation. *Mechanical Systems and Signal Processing* 60-61: 512–534.

Rainieri C, Fabbrocino G and Cosenza E (2011) Near real-time tracking of dynamic properties for standalone structural health monitoring systems. *Mechanical Systems and Signal Processing* 25(8): 3010–3026.

Ren WX and Chen HB (2010) Finite element model updating in structural dynamics by using the response surface method. *Engineering Structures* 32(8): 2455–2465.

Sadhu A, Narasimhan S and Antoni J (2017) A review of output-only structural mode identification literature employing blind source separation methods. *Mechanical Systems and Signal Processing* 94: 415–431.

Sanayei M and Scampoli SF (1991) Structural element stiffness identification from static test data. *Journal of Engineering Mechanics* 117(5): 1021–1036.

Siringoringo DM and Fujino Y (2008) System identification of suspension bridge from ambient vibration response. *Engineering Structures* 30(2): 462–477.

Storn R and Price K (1997) Differential evolution–a simple and efficient heuristic for global optimization over continuous spaces. *Journal of Global Optimization* 11: 341–359.

Sun LM, Zhang W and Nagarajaiah S (2019) Bridge real-time damage identification method using inclination and strain measurements in the presence of temperature variation. *Journal of Bridge Engineering* 24(2): 04018111.

Wang GX, Shao JS, Xu WZ, et al. (2022) Real-time quantitative evaluation on the cable damage of cable-stayed bridges using the correlation between girder deflection and temperature. *Structural Health Monitoring* 21(4): 1483–1500.

Wu ZF, Song YP, Chen H, et al. (2024) A novel mayfly algorithm with response surface for static damage identification based on multiple indicators. *International Journal of Structural Stability and Dynamics* 24(17): 1.

Xia Q, Cheng YY, Zhang J, et al. (2017) In-service condition assessment of a long-span suspension bridge using temperature-induced strain data. *Journal of Bridge Engineering* 22(3): 04016124.

Xu YL and Xia Y (2011) *Structural Health Monitoring of Long-Span Suspension Bridges*. London, UK: Spon Press.

Xia Q, Xia Y, Wan HP, et al. (2020) Condition analysis of expansion joints of a long-span suspension bridge through metamodel-based model updating considering thermal effect. *Structural Control and Health Monitoring* 27(5): e2521.

Xu YL, Chen B, Ng C, et al. (2010) Monitoring temperature effect on a long suspension bridge. *Structural Control and Health Monitoring* 17(6): 632–653.

Yanez-Borjas JJ, Valtierra-Rodriguez M, Camarena-Martinez D, et al. (2020) Statistical time features for global corrosion assessment in a truss bridge from vibration signals. *Measurement* 160: 107858.

Yang DH, Yi TH, Li HN, et al.. (2018) Correlation-based estimation method for cable-stayed bridge girder deflection variability under thermal action. *Journal of Performance of Constructed Facilities* 32(5): 04018070.

Yarnold MT, Moon FL and Emin Aktan A (2015) Temperature-based structural identification of long-span bridges. *Journal of Structural Engineering* 141(11): 04015027.

Yi TH (2021) *Structural Health Monitoring*. Beijing, China: Higher Education Press.

Zhou LR, Chen L, Xia Y, et al. (2020) Temperature-induced structural static responses of a long-span steel box girder suspension bridge. *Journal of Zhejiang University - Science* 21(7): 580–592.

Zhou LR, Wanyan R and Li SJ (2024) Review on convective and radiation heat transfer between bridges and external environments. *Advances in Structural Engineering* 27(8): 1285–1302.

Zhou Y, Xia Y, Chen B, et al. (2020) Analytical solution to temperature-induced deformation of suspension bridges. *Mechanical Systems and Signal Processing* 139: 106568.

Zhou Y, Xia Y, Fujino Y, et al. (2021) Analytical formulas of thermal deformation of suspension bridges. *Engineering Structures* 238: 112228.

Zhou Y, Hao GW, Chen JW, et al. (2024) Long-term deformation monitoring of a steel-truss arch bridge using PSI technique refined by temperature field analysis. *Engineering Structures* 311: 118164.

Zhu QX, Wang H, Xu ZD, et al. (2021) Mapping temperature contours for a long-span steel truss arch bridge based on field monitoring data. *Journal of Civil Structural Health Monitoring* 11: 725–743.

Zuk W (1965) Thermal behaviour of composite bridges-insulated and uninsulated. *Highway Research Record* 76(1): 231–253.